Mechanics & Industry **24**, 41 (2023)
© Y. Feng et al., Published by EDP Sciences 2023
https://doi.org/10.1051/meca/2023039

Mechanics & Industry

Available online at:
www.mechanics-industry.org

REGULAR ARTICLE OPEN ACCESS

Fatigue life prediction of a piercing connector subject to breeze vibration and multi-field coupling

Yu Feng[1,2], Shaolei Wu[2], Kai Wu[2], Wenxin He[1], Zhangbao Wang[1], and Wei Wang[1,*]

[1] School of Mechanical Engineering, Hefei University of Technology, Hefei, PR China
[2] State Grid Anhui Electric Power Co Ltd Electric Power Research Institute, Hefei, PR China

Received: 10 July 2023 / Accepted: 31 October 2023

Abstract. Piercing connectors are widely used in power line erection. However, piercing connectors are susceptible to fatigue failure induced by wind load and multi-field coupling. Therefore, this study aims to predict the fatigue life of piercing connectors. First, the thermal-electrical-mechanical coupling model is created. Second, the electrical contact resistance (ECR) of piercing connectors is experimentally measured and converted into the heat generation rate (HGR) by the thermal equivalence method. Meanwhile, the breeze vibration load (BVL) of the conductor is calculated by the wind vibration theory. Then, the HGR and BVL are applied to perform the multi-field coupling calculation and fatigue life prediction. Finally, the effect of installation torque on the highest temperature, maximum stress, and fatigue life of piercing connectors is analyzed in detail. The results show that the ECR of piercing connectors decreases with the mounting torque, and ultimately tends to be stable. The highest temperature and maximum stress are located on the piercing blade, which is likely to become the failure origin. Within the allowable range of installation torque for piercing connectors, an optimal installation torque exists to minimize the maximum stress fluctuation and prolong the fatigue life.

Keywords: Fatigue life / piercing connector / breeze vibration / multi-field coupling / electrical contact resistance

1 Introduction

With the rapid growth of the demand for electrical energy, this phenomenon brings serious challenges to electricity transmission. High-voltage overhead lines are the key components of power transmission, and piercing connectors are widely used in electrical lines. However, in practice, the failure of a large number of distributed piercing connectors leads to power line failures and even serious fires [1]. The available study exhibits that the failure mode of piercing connectors mainly includes fatigue fracture, fretting wear, and corrosion [2,3]. In recent years, the fierce winds induced by environmental degradation and electric-thermal-mechanical coupling caused by high currents make the piercing connectors more easily fatigue fracture [3]. Therefore, conducting relevant studies on the fatigue life of piercing connectors under the action of multi-field coupling and breeze vibration is necessary.

The finite element method (FEM) was an essential tool for multi-field coupled analysis. For example, Semmar et al. [4] and Technology et al. [5] analyzed the temperature distribution of electrical connectors at room temperature and the structural characteristics of electrical connectors under the temperature loads. He et al. [6] consider the influence of the contact surface state of electrical connectors on the electrical contact resistance (ECR) and heat generation rate (HGR) and performs a coupled evolution analysis of the temperature and the stress-strain field. Xu et al. [7] analyzed the thermal behavior of power connectors and performed a deep study of the thermal-structural coupling failure mechanism. The results show that the multi-physics field coupling of the electrical connector generates significant HGR, which makes the electrical connector subject to a large thermal load. The HGR depends on various factors. Angadi et al. [8] revealed the impact of material and roughness on the temperature rise of electrical connectors via a multi-field coupling model with multi-scale rough surfaces. Israel et al. [9] also built a thermal-electrical coupling model of electrical connectors to explore the transient temperature rise under short circuits. Thus, material properties, surface contact conditions, and current strength have significant effects on the temperature rise of electrical connectors.

Temperature generates a vital impact on the failure of electrical connectors. Sun et al. [10,11] conducted a study on the premature failure of gas-insulated substation (GIS)

* e-mail: weiwang@hfut.edu.cn

Plummer connectors and found that overheating easily occurs when the insertion depth of the connector was insufficient. Moreover, Beloufa et al. [12] investigated the influence of wire diameter on the temperature rise of automotive connectors, and the results showed that a suitable wire diameter can reduce the highest temperature and decrease the failure rate. Tang et al. [13] indicated that the distribution of current in the point-contact contact was circular, which manifests that the heat source and thermal stress distribution were similar. In summary, the temperature rise of electrical connectors under multi-field coupling is a key factor to promote the failure of electrical connectors. Hence, the life prediction of electrical connectors is necessary under multi-field coupling.

The breeze vibration load (BVL) also affects the fatigue life of the piercing connectors. Currently, theoretical studies on the effect of wind load on wire vibration are commonly used, and the most reliable way is the energy balance method proposed by Slethei et al. [14]. With the development of finite element technology, Zhang et al. [15,16] adopted fluid-solid coupling and free vibration modes to analyze the coupled vibration of wind load and wire. The above study shows BVL is an important factor affecting the vibration of the conductor, and reveals the general vibration law of the conductor under different wind load conditions, which lays the foundation for the breeze vibration fatigue analysis of piercing connectors. Kong et al. [17] derived a transmission line breeze vibration fatigue life calculation formula considering the wind speed and wind direction probability distribution based on Miner theory. However, the effect of multi-field coupling is ignored. Therefore, this paper integrates the multi-field coupling and breeze vibration to conduct the fatigue life calculation and prediction studies of the piercing connector.

In the current study, the multi-field coupled model of the piercing connectors is created first. Second, to simulate thermal influence, the ECR was experimentally measured under different installation torques and converted into the corresponding HGR by the thermal equivalence method. Simultaneously, the BVL of the wire is calculated by the wind vibration theory. The HGR and the BVL are loaded into the computational model, and the thermoelectric coupling and structural steady-state and transient analyses of the piercing connector are performed based on the sequential coupling method. Finally, the steady-state highest temperature and maximum stress under different installation torques are obtained. Meanwhile, the effect of installation torque on the fluctuation magnitude of the maximum stress is researched. The fatigue life of the piercing connector in this area is predicted based on the probability distribution of wind speed and direction in a city for 1 yr, as well as Mine's linear cumulative damage criterion. A theoretical basis is provided to formulate suitable maintenance and replacement period for the piercing connector.

2 Multi-field coupling calculation

2.1 Three-dimensional model

The photograph of the piercing connectors is shown in Figure 1. The piercing connectors used for the 10-kV distribution line are comprised of fastening bolts, clip blocks, piercing blades, and so on. The piercing blades contact the wire to form a current conduction path when the tightening force from bolts is applied. The copper set will be twisted off if the tightening force further increases. The design of the copper set facilitates the installation process to avoid uneven force on the piercing blades due to different installation torque. Meanwhile, appropriate installation torque is applied. Eight piercing blades, each with eight piercing contacts are observed. To obtain good electrical and thermal conductivity, the piercing blades are made of copper alloy. The insulating cage is used to maintain the overall structure and protect the internal electrical interface from corrosion and contamination.

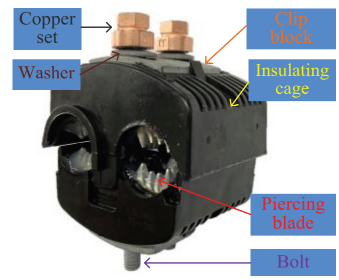

Fig. 1. Piercing connectors.

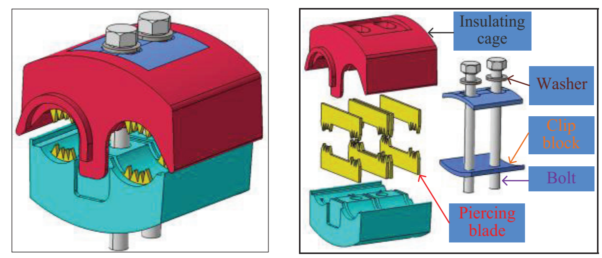

(a) Overall structure (b) Explosive view

Fig. 2. 3D model.

To facilitate the mesh division, an appropriate simplification of piercing connectors (e.g., bolt threads and so on) is necessary. Figure 2 depicts the simplified model, which is $82 \times 62 \times 98$ mm^3 in length, width, and height.

2.2 Material properties

Table 1 lists the mechanical and thermoelectric properties at room temperature [6]. The piercing connectors suffer from a certain temperature rise after power on, but the highest temperature does not exceed 100 °C. Therefore, the influence of temperature rise on the material properties is negligible, and the material properties are assumed to be constant. In general, the contact interface between the blade and wire under preload maintains a strong mutual extrusion effect, which makes the material prone to plastic deformation. Consequently, a nonlinear stress-strain relationship in Figure 3 is adopted to perform the mechanical calculation for the blade and wire.

Table 1. Material properties.

Structure	Piercing blade	Insulation cage	Clip block, washer, bolt	Wire
Material type	Copper alloy	Polybutylene terephthalate	Mild steel	Alumi-num
Young's modulus (MPa)	1.24×10^5	1.42×10^5	2.06×10^5	6.8×10^4
Poisson's ration	0.32	0.35	0.30	0.36
Electrical resistivity $(\mathrm{cm} \cdot \mu\Omega)$	1.65	/	2.85	2.65
Coefficient of thermal conductivity $(\mathrm{W} \cdot \mathrm{m}^{-1} \cdot {}^{\circ}\mathrm{C}^{-1})$	394	0.34	64.8	222
Specific Heat Capacity $(\mathrm{J} \cdot \mathrm{g}^{-1} \cdot {}^{\circ}\mathrm{C}^{-1})$	0.46	1.46	0.88	0.88
Density $(\mathrm{g} \cdot \mathrm{cm}^{-3})$	8.9	2.5	7.85	2.7

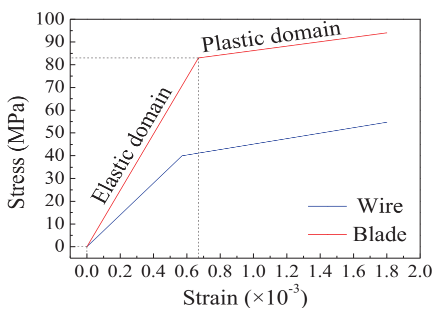

Fig. 3. The mechanical properties.

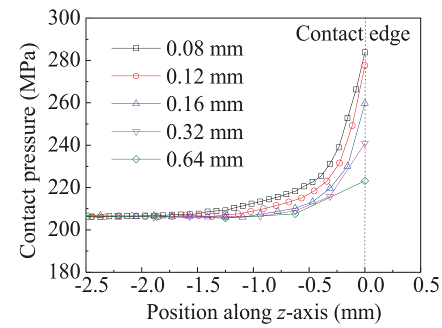

Fig. 4. Contact pressure at contact edge versus mesh size.

2.3 Computational model

The 3D hexahedral element Solid 45 is used to conduct mechanical calculations for the puncture blades, clip blocks, and wires, and the tetrahedron element Solid 95 is employed for the insulating cage. Solid 45 and 95 are replaced by a 3D coupled-field Solid 226 in the thermo-electric analysis. To facilitate the preload application, a preload element Prets 179 is created in the middle section of the bolt. Meanwhile, the 3D contact elements Contact 174 and Target 170 are defined on the surface of the piercing blade and the wire. The contact elements possess the same degrees of freedom (DOFs) as the body element. To guarantee the accuracy of the contact calculation, the Gaussian integration point is selected as the contact detection point. In addition, appropriate allowable penetration and friction coefficient of 0.3 are required. The default convergence tolerance factor of 0.1 is adopted in ANSYS. A factor of less than 0.2 is also recommended if convergence is still difficult.

The 3D contact elements are used to simulate heat and electricity conductance between the contact surfaces. Therefore, the thermal contact conductivity (TCC) and electrical contact conductivity (ECC) described in detail in ANSYS help are important. The heat flux q is defined as the product of TCC and temperature difference ΔT. More apparently, a larger TCC implies that the contact is more perfect, and the effect of ECC has a similar law. The literature [18] indicates the order of magnitude of TCC is 10-10^6 $\mathrm{W} \cdot \mathrm{mm}^{-2} \cdot {}^{\circ}\mathrm{C}^{-1}$ for perfect thermal contact. Accordingly, in this paper, the contact is also assumed to be perfect, and a larger TCC of 10^6 $\mathrm{W} \cdot \mathrm{mm}^{-2} \cdot {}^{\circ}\mathrm{C}^{-1}$ is defined. References [19,20] state that ECC is 100-10^6 $\mathrm{S} \cdot \mathrm{mm}^{-2}$ in perfect electrical contact. Thus, ECC is 10^6 $\mathrm{S} \cdot \mathrm{mm}^{-2}$.

In light of the experience of finite element analysis, smaller mesh sizes are beneficial to obtain the stress concentrations at the contact edges more accurately, but a longer computation time is required. Accordingly, the mesh size needs to be optimized. Figure 4 demonstrates the contact pressure at the contact edge versus the grid size. The lesser the grid dimension, the greater the contact pressure at the contact edge and the more time consuming the process. Furthermore, the contact pressure at the contact edge varies slightly when the grid size is less than 0.12 mm. Thus, the minimum element size is 0.12 mm. The grid size away from the contact edge is 1.50 mm. After the completion of grid division, Figure 5 shows the computational model with 1,245,325 nodes and 956,359 elements.

2.4 Multi-field coupling calculation program

The direct coupling method and load transfer method are used to perform the multi-field coupling calculations for different research objects [21]. Although the numerical calculations are executed on a high-performance workstation that has a 3.6 GHz Intel(R) Core(TM) i9-9900K CPU and 64 GB RAM, the computational efficiency is low using

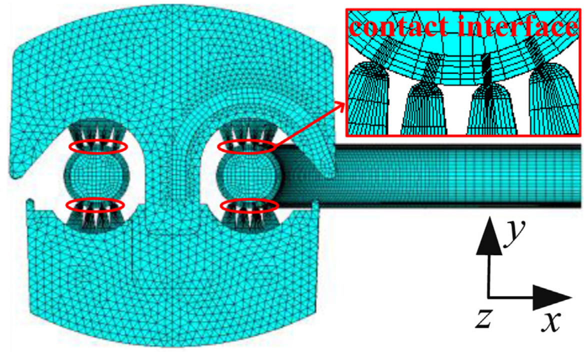

Fig. 5. Computational model.

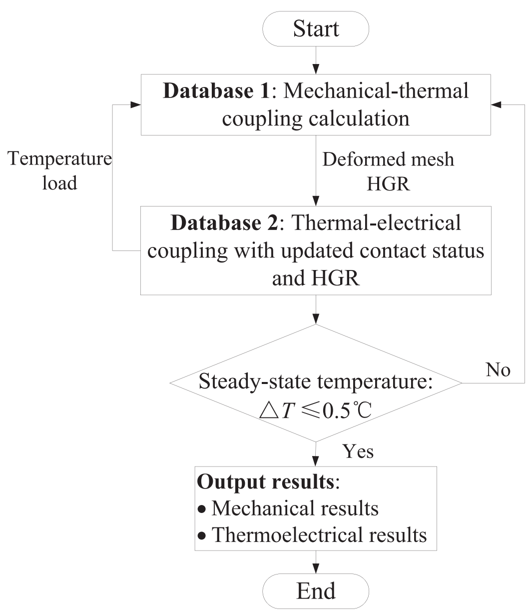

Fig. 6. Multi-field coupling calculation program.

the direct coupling method. Consequently, the load transfer method is employed. To consider the bi-directional coupling effect between multiple fields, an improved load transfer method is proposed. Figure 6 depicts the multi-field coupling calculation procedure. Table 2 represents the calculation time for each method. Although the improved load transfer method is more time-consuming than the load transfer method, the computational efficiency is acceptable and the accuracy is significantly improved.

2.5 Boundary conditions

Heat transfer mainly includes heat conduction, heat convection, and thermal radiation, of which heat conduction is the most basic [22]. Heat conduction follows Fourier's law:

$$q = -\lambda \frac{dT}{dx} \tag{1}$$

Table 2. Comparison of computation time.

Method	Calculation time
Direct coupling method	5 weeks
Load transfer method	6.5 h
Improved load transfer method	32.5 h

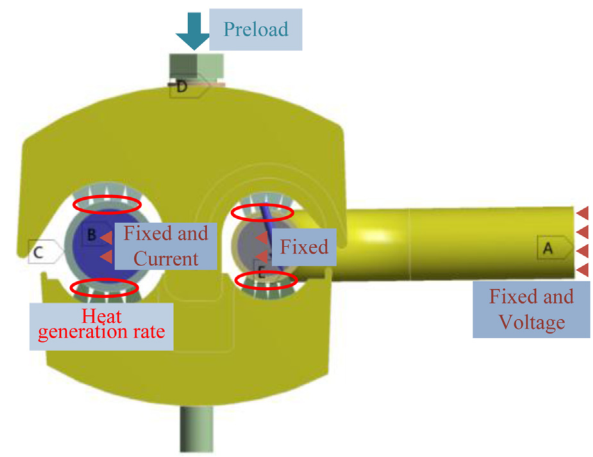

Fig. 7. Boundary conditions of the computational model.

where q represents the heat flux, λ expresses the heat transfer coefficient, T means the temperature and x denotes the position.

The heat convection follows Newton's law [18] expressed as follows:

$$\phi = h_c A\left(T_w - T_f\right) \tag{2}$$

where φ is the heat flow, h_c represents the coefficient, A expresses the area, and T_w and T_f are surface and fluid temperature, respectively.

Thermal radiation efficiency is the lowest in the atmosphere [23]. The effect of heat radiation is very small and even ignorable. Thus, the film coefficient of 4.85 $\mathrm{W \cdot m^{-2} \cdot {}^{\circ}C^{-1}}$ at a room temperature of 22 °C is defined for the outside surface of the piercing connector.

First, the mechanical-thermal coupling calculation is performed based on the preload of 26 N · m and fixation constraints. Then, the thermoelectric analysis is executed by applying the deformed mesh, voltage, current, and HGR. Then, the mechanical-thermal coupling computation is performed again to realize the cyclic load transfer. The cyclic process does not exist until the global temperature reaches a steady state. Finally, the temperature and wind loads are loaded to carry out the transient mechanical analysis. Figure 7 gives the detailed boundary conditions.

The transient results are imported into the nCode, a fatigue analysis software, after the mechanical calculation. The S-N curve of the material and mean stress correction of

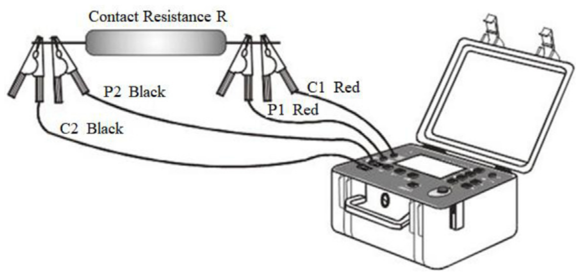

(a) Experimental circuit

(b) Micro-ohmmeter

Fig. 8. Experimental circuit and measurement instrument of ECR.

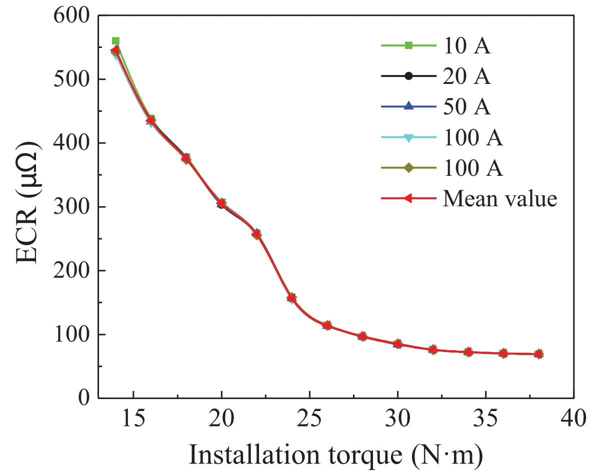

Fig. 9. Relationship between ECR and installation torque.

the Goodman equation are defined. The damage factor and fatigue life of the piercing connector are then calculated based on the Mine linear cumulative damage criterion.

2.6 Electrical contact resistance equivalent treatment

Figure 8 shows the experimental circuit and apparatus. Thereinto, the micro-ohmmeter based on the four-wire method possesses sufficient measure accuracy [24]. The ECR under different installation torques is measured (Fig. 9). The average value of three measurements under the same conditions is taken as the final result to reduce the measurement error.

Figure 9 shows that the ECR decreases nonlinearly with the increase of the installation torque. The ECR shows a significant change in the installation torque under the installation torque of <30 N · m. The ECR tends to plateau when the installation torque is >30 N · m. This is mainly because the piercing blade is not completely in contact with the wire under a smaller torque, and the better the contact as the torque increases. The contact effect is not significantly improved, which stabilizes the ECR when the torque increases to a certain level.

The main heat source is from ECR, and an accurate heat equivalence method is necessary [25]. For the piercing connector model, the ECR exists only at the contact area, so the equivalent HGR q is calculated as in equation (3):

$$q = \frac{p}{s} = \frac{i^2 R_c}{2S} \tag{3}$$

where i denotes the current intensity, R_c is the ECR, and S expresses the total contact area.

Assuming the current strength of 290 A, the real contact areas under different mounting torque are obtained via the mechanical simulation, and then the HGR is defined based on the experimentally measured contact resistance and the numerically calculated real contact areas to perform the subsequent thermal-electrical coupling calculations.

3 Breeze vibration characteristics

3.1 Wind vibration theory

The phenomenon of the "Karman vortex" indicates that the long-span conductor is always in a steady vibration state [26]. According to the Karman vortex properties by Kalman and Storroha, the vibration frequency of the cylinder is related to the wind speed as follows:

$$f = S\frac{v}{D} \tag{4}$$

where f is vortex frequency (in Hertz), v is wind speed (in meters per second), D is the column diameter, and S represents the Strohal number (value range, 0.185–0.21).

The "Karman vortex" induced by the breeze vibration of the wire can be calculated using the energy balance method [27], mainly considering the wind load input energy, damping energy consumption, and energy consumption of the anti-vibrator:

$$P_w = P_c + P_d \tag{5}$$

where P_w is the wire wind load input power, P_c denotes the damping energy consumption, and P_d represents the energy consumption of the anti-vibrator.

In this work, the 10-kV distribution line has no anti-vibration measures, so $P_d = 0$. The wind load input power P_w uses the fitting formula proposed by Diana and Falco:

$$\begin{cases} P_w = \beta_w \left(\frac{y}{D}\right)^{2a_1} \left(\frac{y}{D}\right)^{a_2} e^{a_3} f^3 D^4 (y < 0.6D) \\ P_w = 27.51 \beta_w f^3 D^4 (0.6 < y < D) \\ P_w = 0 (y \geq D) \end{cases} \tag{6}$$

where a_1, a_2, and a_3 are 0.0526, 1.4074, and 4.0324, respectively; y is the single amplitude; and D is the wire diameter.

The actual environment may influence wind energy. An inhomogeneity factor β_w is introduced to correct the wind input power [28], as calculated by the following equation:

$$\beta_w = \frac{1}{\sqrt{1 + \left(\frac{I_v}{I_L}\right)^2}} \tag{7}$$

where I_L is the locking constant, 0.09, V_w is the average wind speed, σ_v is the standard deviation of wind speed, and I_v is the turbulence of the wind at the suspension point of the wire, $I_v = \sigma_v / V_w$, or estimated by the following formula:

$$I_v = 2.45\sqrt{k}\left(\frac{Z_r}{Z}\right)^{\alpha} \tag{8}$$

where k is the ground friction coefficient, α implies a terrain-related constant, Z_r represents the reference height, and Z denotes the height of the suspension point. In this work, k and α are 0.004 and 0.15, respectively.

The damping energy consumption P_c is mainly from the internal friction loss between the wire strands. The semi-empirical formula can be utilized:

$$P_c = 1.07 \times 10^6 E_{eq} \sqrt{K_D} K_S K_0 L \frac{D^{4.5} f^{6+\beta} \left(\frac{Y_0}{2}\right)^{2.5}}{V_c{}^5} \tag{9}$$

where K_0 and β are 0.0042 and 0.4256, respectively. E_{eq} is the elastic modulus of the wire, K_D is the empirical factor, 0.54, K_S is the maximum bending stiffness discount factor, 0.5, L is the span of a wire, D is the diameter of a wire, and V_c is the wave speed of the wire, $V_c = \sqrt{T/m}$.

In this work, the overhead wire with the type of JKLYJ-240 is regarded as an example, with a span of 70 m, an outer diameter of 26.8 mm, and a rated breaking force of 34.68 kN. The breeze vibration frequency is generally 5–150 Hz [29] and the maximum amplitude of the wire induced by breeze vibration does not exceed the diameter of the conductor itself. Thus, the minimum and maximum vibration frequencies are 12 Hz and 70 Hz, respectively. Based on the energy balance method, the relationship between the amplitude and frequency of the wire is obtained. Figure 10 shows that the wire breeze vibration amplitude nonlinearly decreases with the frequency increasing to 40 Hz, a critical frequency. Under low frequency, wind load vibration will make the piercing connector withstand the larger vibration load.

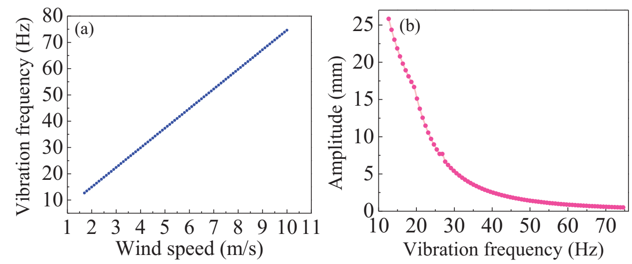

(a) Frequency vs. wind speed (b) Amplitude vs. frequency

Fig. 10. Relation between conductor vibration frequency, wind speed, and amplitude.

3.2 Number of wind load fluctuations

The relationship between wind speed and wind direction meets statistical laws in a certain period (e.g., Weibull, Pearson). In this paper, the Weibull function is used [30]:

$$p(V \leq V_C) = 1 - \exp\left[-(V_C/c_w)^{k_w}\right]. \tag{10}$$

This equation represents the probability when the wind speed is less than V_C in the statistical time. k_w and c_w are the shape and scale parameters, respectively. The parameters are calculated as follows:

$$k_w = 0.74 + 0.19v \tag{11}$$

$$c_w = v/\Gamma(1 + 1/k_w) \tag{12}$$

where v is the annual average wind speed.

Combining equation (4), equation (10) has the following form:

$$p(f \leq f_C) = -\exp\left[-(f_C D/S c_w)^{k_w}\right]. \tag{13}$$

In this paper, the extracted frequency range is uniformly divided into N frequency bands, and then the probability of the i frequency band is calculated as follows:

$$p(f_{Ci1} \leq f_i \leq f_{Ci2}) = \exp\left[-(f_{Ci1} D/S c_w)^{k_w}\right] - \exp\left[-(f_{Ci2} D/S c_w)^{k_w}\right]. \tag{14}$$

The total time of the i frequency band in a year is:

$$t_i = 3.1536 \times 10^7 \times \left\{\exp\left[-(f_{Ci1} D/S c_w)^{k_w}\right] - \exp\left[-(f_{Ci2} D/S c_w)^{k_w}\right]\right\}. \tag{15}$$

The total number of vibrations is:

$$n_i = t_i \times f_i. \tag{16}$$

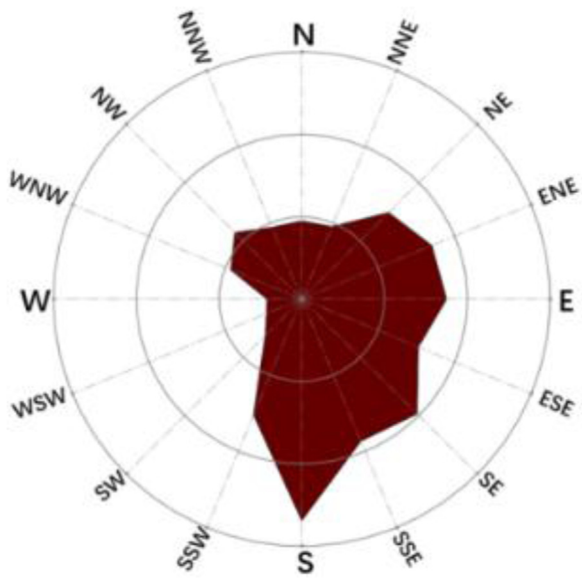

Fig. 11. Wind rose chart in a city.

The total time for which the vibration occurs is:

$$t=\sum_{i=1^N}t_i=3.1536\times10^7\times\sum_{i=1}^{N}\left\{\exp\left[-(f_{Ci1}D/Sc_w)^{k_w}\right]-\exp\left[-(f_{Ci2}D/Sc_w)^{k_w}\right]\right\}. \tag{17}$$

Distribution line wire breeze vibration is not only related to the wind speed but also the wind direction. Stable breeze vibration of the wire occurs when the wind direction is at an angle of 45°–90° with the wire [31]. Only the stable breeze vibration is considered for the convenience of analysis. Moreover, Figure 11 depicts the annual wind rose diagram in a city, and the wind direction of the city is mainly concentrated in the south. Therefore, the more stable vibrations occur in the wire when the conductor is erected along the east-west direction, and the probability of stable vibration throughout the year is about 67.59%.

Assuming an average wind speed $V_C = 6\ \mathrm{m\cdot s^{-1}}$, and k_w and c_w are 2.07 and 7.9, respectively, by equations (11) and (12). Combined with the relationship between amplitude and frequency in Figure 9, the probability of vibration, vibration time, and the number of vibrations are calculated every 5 Hz, and the results are listed in Table 3.

Table 3. Relative parameters of vibration in each frequency band throughout the year.

Vibration frequency (Hz)	Vibration probability	Vibration time (h)	Number of vibrations ($\times10^7$)
15–19	0.0232	203.47	1.0988
20–24	0.029	254.07	1.8293
25–29	0.0337	295.34	2.6581
30–34	0.0372	325.79	3.5186
35–39	0.0394	344.71	4.3433
40–44	0.0402	352.14	5.0708
45–49	0.0398	348.83	5.6508
50–54	0.0384	336.03	6.0486
55–59	0.0360	315.50	6.2469
60–64	0.0330	289.15	6.2458
65–69	0.0296	259.00	6.0606

4 Results and discussions

4.1 Analysis of temperature rise

The steady temperature distribution is shown in Figure 12 when the installation torque and current intensities are 24 N · m and 290 A, respectively. The temperature of the piercing blade is the highest, ~55.44 °C. The temperature of the cage is the lowest, ~35.14 °C, with a temperature difference of 20.33 °C. The whole temperature distribution is extremely uneven. However, the temperature distribution of the piercing blade is more uniform, which is because of the good thermal conductivity of the piercing blade. This internal temperature concentration phenomenon is not conducive to the long-term operation of piercing connector, facilitating aging failure. Therefore, the cage material possesses, as far as possible, good thermal conductivity and strength.

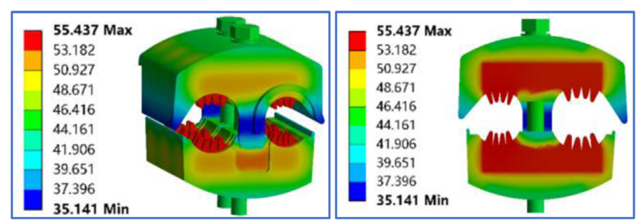

(a) Axonometric view (b) Cutaway view

Fig. 12. Temperature distribution.

Figure 13 explains the maximum, average, and minimum temperatures of the piercing connector versus mounting torques. The temperatures show a decreasing trend and ultimately stabilize, which is consistent with the ECR trend. The maximum temperature of the piercing connector under 32 and 14 N · m is 49.03 and 86.42 °C, respectively, when the current intensity is 290 A. The temperature difference reached 37.39 °C, which illustrates that the installation torque has an important influence on the temperature rise. Reference [32] shows that the highest temperature allowed for the piercing connector in long-term operation should not exceed 75 °C. Combined with the numerical results, the installation torque should be >18 N · m within the rated current intensity.

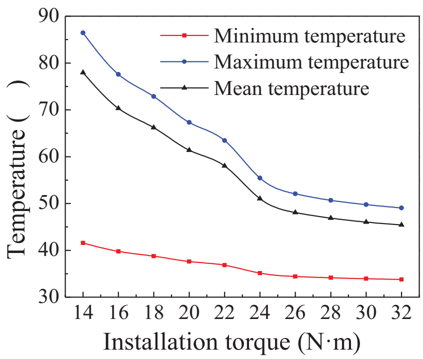

Fig. 13. Maximum temperature vs. installation torque.

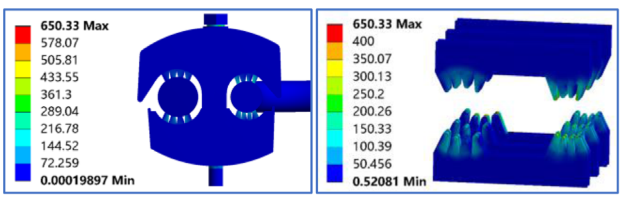

(a) Overall stress distribution (b) Blade stress distribution

Fig. 14. Von Mises stress distribution.

4.2 Analysis of mechanical results

Figure 14 expresses the overall von Mises stress distribution when the piercing connector is subjected to the preload of 24 N · m only. The maximum equivalent stress located on the blade is 650.33 MPa. Therefore, the strength of the blade is the weakest in the overall structure. The maximum equivalent stress exceeds the yield strength, so the definition of a nonlinear stress–strain relationship is necessary.

Figure 15 shows the maximum von Mises stress versus time under breeze vibration and different installation torques. After the installation completion, the maximum equivalent stress reaches the maximum at 0.03 s and increases with the installation torque increasing. The maximum stress reaches 860 MPa under the installation torque of 32 N · m. The maximum stress starts to fluctuate induced by the temperature and breeze vibration. Under the installation torque of <28 N · m, the maximum stress fluctuates around a certain level, but the trend of the maximum stress fluctuation under different installation torques is similar. Meanwhile, the stress fluctuation curve is roughly at the same level, and only a difference in fluctuation amplitude is observed when the installation torque is >28 N · m. The larger the installation torque, the smaller the stress fluctuation amplitude, which is due to the suppression of stress fluctuations by a large mounting load. Thus, the wind load vibration has less influence on the maximum stress fluctuation under the large installation torque condition.

For the effect of breeze vibration on the stress distribution of the piercing connector, Figure 15 depicts the relationship between the maximum equivalent stress growth, fluctuation amplitude, and installation torque. The fluctuation amplitude is a difference value between the peak and valley value of the maximum stress fluctuation curve, and the steady-state mean value is calculated during the stable fluctuation period.

Figure 16a explains that the maximum stress fluctuation amplitude reduces gradually with the increase of the mounting torque. Moreover, a significant local abrupt change is observed, which may be due to the change of the ECR caused by the change of the mounting torque, and the weakening of the interaction between the multi-field coupling. The larger installation torque, >24 N · m, significantly reduces the maximum stress fluctuation amplitude. Hence, the stress fluctuation amplitude is less affected by the breeze vibration under the larger installation torque. In addition, Figure 16b illustrates that the steady-state mean value tends to increase with the installation torque increase. The steady-state mean value increment is the largest, ~91.1 MPa when the mounting torque increases from 26 to 28 N · m. However, a larger mounting load will noticeably reduce the stress fluctuation amplitude, and the smaller stress amplitude is then beneficial to prolonging the fatigue life. In summary, the results of the mechanical analysis show that the suitable installation torque range is >24 N · m.

4.3 Fatigue life analysis

The fatigue life of the piercing connector under wind speed of 6 $m \cdot s^{-1}$ and installation torque of 24 N · m is obtained through ANSYS nCode. Figure 17 interprets the fatigue life of the piercing blade caused by the breeze vibration. The number of cycles for a node with the shortest fatigue life is extracted, ~9.489×10^9. The simulation results are based on 20 complete cycles. Thus, the minimum number of cycles for the piercing blade at a wind speed of 6 m/s is as follows:

$$N = 20 \times 9.489 \times 10^9 = 1.896 \times 10^{11}. \quad (18)$$

The relationship between the frequency, amplitude, and wind speed exists. Therefore, the fatigue life of the piercing connector is predicted with the middle value of different frequency intervals. Table 4 depicts the number of breeze vibrations under the corresponding frequency. The second and third columns are the probability and total time of load fluctuations under the different breeze vibration frequency bands in a year, and the fourth column is the maximum number of load fluctuations that the piercing connector can withstand.

According to Mine theory, the fatigue life of the piercing connector because of the cyclic structural stress and thermal stress is calculated based on equations (19) and

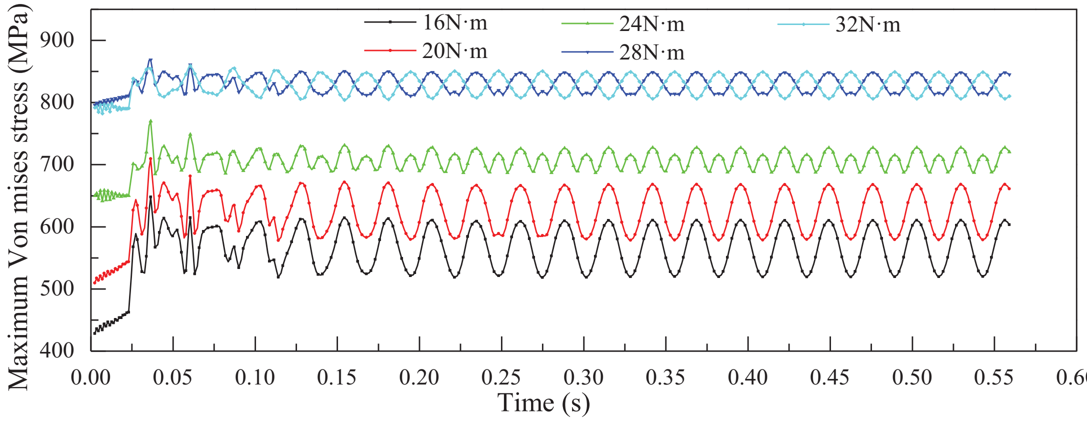

Fig. 15. Maximum von Mises stress as a function of mounting torque.

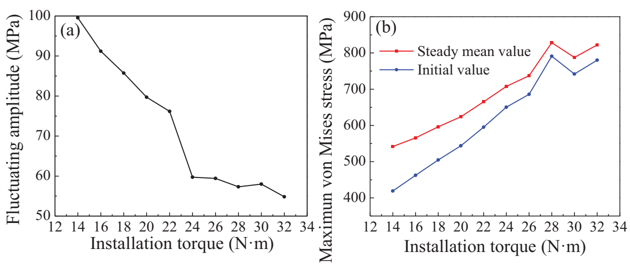

Fig. 16. Effect of mounting torque on the maximum stress fluctuation. (a) Stress fluctuation amplitude vs. mounting torque (b) The maximum von Mises stress growth versus mounting torque.

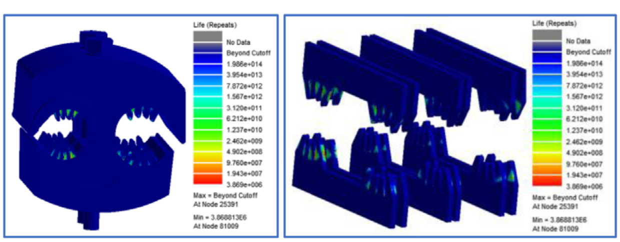

(a) Overall lifetime cloud (b) Piercing blade lifetime cloud

Fig. 17. Fatigue life of the piercing connector.

(20) [17]:

$$D = \sum_{i=1}^{11} \frac{n_i}{N_i} \tag{19}$$

$$L = 1/D \tag{20}$$

Table 4. The number of load fluctuations of the piercing connector.

Serial number	Vibration frequency (Hz)	Number of load fluctuations ($\times 10^7$)	Total maximum load fluctuation ($\times 10^7$)
1	15–19	1.0988	20.82
2	20–24	1.8293	92.78
3	25–29	2.6581	1026.58
4	30–34	3.5186	7518
5	35–39	4.3433	9832
6	40–44	5.0708	11906
7	45–49	5.6508	17362
8	50–54	6.0486	17766
9	55–59	6.2469	18960
10	60–64	6.2458	19178
11	65–69	6.0606	19216

where n_i is the number of load fluctuations in a frequency band, N_i is the total number of maximum load fluctuations in every frequency band, D is the total damage factor, and L is the fatigue life of the piercing connector.

The total fatigue damage factor due to breeze vibration in a city is 0.078 based on the above analysis and calculation, and the corresponding fatigue life is about 12.82 yr.

5 Conclusion

In this work, a numerical method is used to predict the fatigue life of the piercing connector under the breeze vibration and multi-field coupling. The conclusions are as follows:

– The ECR of the piercing connector decreases with the increase in installation torque, while the highest temperature is also lower, which is beneficial to improving the working condition. The temperature of the piercing blade is the highest. Therefore, temperature monitoring should be placed on the blade. Furthermore, the insulation cage should possess good thermal conductivity to optimize internal heat dissipation.
– The highest temperature of the piercing connector increases with the decrease of the installation torque or the increase of the current intensity. The highest temperature of $<75\,°\mathrm{C}$ is required to ensure the stable operation of the 10-kV distribution line. Therefore, the minimum installation torque is 18 $\mathrm{N \cdot m}$.
– The larger the installation torque of the piercing connector, the higher the maximum von Mises stress. However, the larger installation torque can reduce the maximum stress fluctuation amplitude caused by breeze vibration, especially $>24\,\mathrm{N \cdot m}$. The maximum von Mises stress fluctuation amplitude drops abruptly to prolong the fatigue life.
– According to the wind speed and wind direction statistics in a city throughout the year, the total fatigue damage factor of the piercing connector caused by breeze vibration is 0.078, and the fatigue life is about 12.82 yr. The results provide scientific guidance for maintenance and replacement.

Conflict of interest

The authors declare no conflict of interest.

Funding

This work is supported by the National Natural Science Foundation of China (Grant No. 51975174) and the Science and Technology Project of State Grid Corporation of China (Grant No. 52120520005B).

References

[1] X. Dong, F. Qu, Y. Li et al., Simulation analysis and verification on three-dimensional temperature field of strain clamps for overhead lines, J. Southwest Jiaotong Univ. **54**, 997–1004 (2019)
[2] S.V. Angadi, R.L. Jackson, V. Pujar et al., A comprehensive review of the finite element modeling of electrical connectors including their contacts, IEEE Trans. Compon., Packaging Manuf. Technol. **10**, 836–844 (2020)
[3] S. Lalonde, R. Guilbault, S. Langlois, Numerical analysis of ACSR conductor-clamp systems undergoing wind-induced cyclic loads, IEEE Trans. Power Deliv. **33**, 1518–1526 (2018)
[4] N. Semmar, C. Georges, L.C. Boulmer, Thermal behaviour of electric connector coating irradiated by a laser beam, Microelectronics J. **33**, 705–710 (2022)
[5] S. Robertson, M. Technology, A finite element analysis of the thermal behavior of contacts, IEEE Trans. Compon., Hybrids Manuf. Technol. **5**, 3–10 (1982)
[6] W. He, W. Wang, Z. Wang et al., Simulation and experimental study on temperature rise characteristic of a piercing connector, IEEE Trans. Compon., Packaging Manuf. Technol. **12**, 512–21 (2022)
[7] X. Wang, L.J. Xu, Finite element model analysis of thermal failure in connector, J. Zhejiang Univ. Sci. **A 3**, 397–402 (2007)
[8] S.V. Angadi, R.L. Jackson, S.Y. Choe et al., A multi-physics finite element model of a 35 A automotive connector including multiscale rough surface contact, 56th IEEE Holm Conference on Electrical Contacts. Charleston, SC, USA, 4-7 October 2010
[9] T. Israel, S. Schlegel, S. Großmann et al., Modelling of transient heating and softening behaviour of contact points during current pulses and short circuits, 2019 IEEE Holm Conference on Electrical Contacts, Milwaukee, WI, USA, 14-18 September 2019
[10] G.X. Sun, X.Y. Guan, X.C. Jin, Thermal failure analysis of bus joint of gas insulated switchgear based on multi-field coupling calculation, High Voltage Technol. **40**, 3445–3451 (2014)
[11] G.X. Sun, N.Q. Shu, X.W. Wu, Finite element calculation of contact temperature rise of gas insulated bus contact based on multi-physical field coupling, Trans. China Electrotech. Soc. **28**, 408–413 (2013)
[12] A. Beloufa, The effect of cable section on the variation of power automotive connector temperature, IEEE Trans. Compon., Packaging Manuf. Technol. **9**, 1020–1028 (2019)
[13] Z.L. Tan, S. Chen, W.M. Guan, Thermal-electro-mechanical coupling analysis and experimental study of AgNi10 contact material in closed contact stage, Rare Metal Mater. Eng. **41**, 276–280 (2012)
[14] G. Diana, M. Falco, On the forces transmitted to a vibrating cylinder by a blowing fluid, Meccanica **6**, 9–22 (1971)
[15] M. Zhang, G. Zhao, L. Wang, Wind-induced coupling vibration effects of high-voltage transmission tower-line systems, Shock Vib. **2017**, 1205976 (2017)
[16] M. Zhang, G. Zhao, J. Wang, Study on fluid-induced vibration power harvesting of square columns under different attack angles, Geofluids **2017**, 6439401 (2017)
[17] D.Y. Kong, Li, X.H. Long, Analysis of factors influencing breeze vibration fatigue life of transmission line, J. Wuhan Univ. Technol. **32**, 53–57 (2010)
[18] J.J. Gou, X.J. Ren, Y.J. Dai et al., Study of thermal contact resistance of rough surfaces based on the practical topography, Comput. Fluids **164**, 2–11 (2018)
[19] W. He, Y. Feng, S. Wu et al., Effect of elastoplastic thermal softening on thermal contact resistance based on the dual-load transfer coupling method, Int. J. Therm. Sci. **183**, 1–15 (2023)
[20] Z. Wan, H.P. Wang, M. Wang et al., Numerical simulation of resistance spot welding of Al to zinc-coated steel with improved representation of contact interactions, Int. J. Heat Mass Transf. **101**, 749–763 (2016)
[21] W. He, Y. Feng, S. Wu et al., Mechanical-thermal-electrical coupling modeling and temperature rise characteristic of a parallel groove clamp with improved representation of contact interactions, IEEE Trans. Compon., Packaging Manuf. Technol. **13**, 356–364 (2023)
[22] Y.J. Dai, X.J. Ren, Y.G. Wang et al., Effect of thermal expansion on thermal contact resistance prediction based on the dual-iterative thermal-mechanical coupling method, Int. J. Heat Mass Transf. **173**, 1–15 (2021)

[23] W. He, Y. Feng, S. Wu et al., Effect of elastoplastic thermal softening on electrical contact resistance based on the dual-iterative coupling method, IEEE Trans. Dielectr. Electr. Insul. **30**, 11–19 (2023)

[24] I. Theodosoglou, A. Papagiannakis, B. Wiecek et al., Electrothermal analysis and temperature fluctuations prediction of overhead power lines, Int. J. Electr. Power Energy Syst. **87**, 198–210 (2017)

[25] J.R. Riba, C. Abomailek, A.G. Mancini et al., A 3D-FEM-based model to predict the electrical constriction resistance of compressed contacts, Measurement **114**, 44–50 (2018)

[26] T. Sugimoto, Y. Sasaki, Fatigue life of structural plywood under two-stage panel shear load: a new cumulative fatigue damage theory, J. Wood Sci. **53**, 211–217 (2007)

[27] Y. You, L. Zhang, L. Zhang, Study on finite element analysis of breeze vibration of transmission lines based on three-node cable elements, IOP Conf. Ser.: Earth Environ. Sci. **170**, 1–8 (2018)

[28] M.L. Liu, H.K. Lu, K. Luo, Numerical simulation of wind-induced response of transmission tower line system under real mountainous terrain conditions, J. Vib. Shock **39**, 232–239 (2020)

[29] B. Chen, X.X. Song, J.B. Wu, Research progress on mechanical model of transmission tower line system, Eng. Mech. **38**, 1–21 (2021)

[30] T. Li, Q. Wang, D.G. Wu, Wind tunnel test and wind-induced response analysis of 1000 kV transmission tower under typhoon wind field, J. Electr. Power Sci. Technol. **36**, 76–82 (2021)

[31] W.B. Buchanan, Vibration analysis-transmission line conductors, Electr. Eng. **53**, 1478–1485 (1934)

[32] H.Y. Yu, R. Li, C.Z. Zhu, Insulated Wire Connection and Lightning Protection Technology of Distribution Network, China Electric Power Press, Beijing, 2012

Cite this article as: Y. Feng, S. Wu, K. Wu, W. He, Z. Wang, W. Wang, Fatigue life prediction of a piercing connector subject to breeze vibration and multi-field coupling, Mechanics & Industry **24**, 41 (2023)